AIP | Applied Physics Letters

On the elastically coupled magnetic and ferroelectric domains: A phase-field model

T. N. Yang, Jia-Mian Hu, C. W. Nan, and L. Q. Chen

Citation: Applied Physics Letters **104**, 202402 (2014); doi: 10.1063/1.4875719
View online: http://dx.doi.org/10.1063/1.4875719
View Table of Contents: http://scitation.aip.org/content/aip/journal/apl/104/20?ver=pdfcov
Published by the AIP Publishing

On the elastically coupled magnetic and ferroelectric domains: A phase-field model

T. N. Yang,[1,a)] Jia-Mian Hu,[1,2] C. W. Nan,[2] and L. Q. Chen[1,2]
[1]*Department of Materials Science and Engineering, The Pennsylvania State University, University Park, Pennsylvania 16802, USA*
[2]*State Key Lab of New Ceramics and Fine Processing, School of Materials Science and Engineering, Tsinghua University, Beijing 100084, China*

(Received 4 February 2014; accepted 28 April 2014; published online 20 May 2014)

A phase-field model is developed to study local elastic coupling between magnetic and ferroelectric domains that show one-to-one pattern match. A multiferroic layered heterostructure of $Co_{0.4}Fe_{0.6}/BaTiO_3$ is considered as an example. Dynamics of the local elastic coupling is investigated by simulating a time-dependent electric-field driven changes in local magnetization/polarization/strain distributions and by comparing the associated velocities of the magnetic and ferroelectric domain walls. It is found that the electric-field-driven dynamic magnetic domain evolution manifests itself as an alternating occurrence of local magnetization rotation and coupled motion of magnetic and ferroelectric domain walls with almost identical velocities.
 [http://dx.doi.org/10.1063/1.4875719]

The scaling law for ferroics[1,2] indicates that the domain width of magnets and ferroelectrics become comparable only when the thickness of ferroelectrics is much larger. Indeed, it has been recently demonstrated in multiferroic layered heterostructures with magnetic thin films directly grown on ferroelectric (FE) $BaTiO_3$ (BTO) substrates[3–10] that the domains in an as-grown magnetic thin film have not only the same width but also a surprising collinear alignment with the contacted FE domains. This further enables a precise control over the magnetic domain wall motion by electrically driving its elastically coupled FE domain wall.[11,12] Such one-to-one match between magnetic and FE domains offers new opportunities for the creation of periodic magnetic domain patterns used for magnonic devices,[13] and particularly, the low-power spintronic devices based on electro-strain-driven magnetic domain orientation[14,15] or domain wall propagation.[16,17]

Theoretically, both *ab initio* calculations[8] and continuum-scale models[9] have been employed to describe the variations in the average magnetization as a function of electric field and/or temperature for such multiferroic magnetic/FE heterostructures. However, a rigorous three-dimensional (3D) mesoscale[18] model that can simulate the dynamic evolution of these elastic coupled magnetic and FE domains under external magnetic/electric field, is still lacking.

In this Letter, a phase-field model is developed to study the dynamics of such local elastic coupling between magnetic and FE domains in multiferroic heterostructures. We simulate the evolution of both types of domains upon applying an electric field to the heterostructure including field-driven changes in domain morphology and domain wall velocity. The simulation results agree with existing experimental observations. For illustration, we choose a model heterostructure with a polycrystalline $Co_{0.4}Fe_{0.6}$ (CoFe) magnetic film deposited on a BTO single crystal substrate that initially has a periodic in-plane FE domain pattern.[3–5]

To overcome the challenge to model the large discrepancy between the thicknesses of the BTO substrate (μm ~ mm) and the CoFe film (~nm), the phase-field modeling is carried out in two steps to mostly capture the mechanical boundary conditions in real systems: (1) simulating FE domain evolution and associated ferroelastic strain distribution in bulk BTO substrate [Fig. 1(a)]; (2) simulating magnetic domain evolution in CoFe film within a film-substrate system [Fig. 1(b)],[19] where effects of ferroelastic strains from the BTO substrate are considered by employing a modified elastic boundary condition.

In Step 1, the total size of the bulk BTO crystal is set as $800 \times 800 \times 400\,nm^3$, which is discretized into a three-dimensional (3D) array of $160 \times 160 \times 80$ cells. The FE domain structure is described with a local polarization field $\mathbf{P}(\mathbf{x})$, where $\mathbf{x}$ is the position vector.

Temporal evolution of the polarization field follows the time-dependent Ginzburg-Landau equation, i.e.,

$$\frac{\partial \mathbf{P}}{\partial t} = -L_P \frac{\delta F}{\delta \mathbf{P}}, \tag{1}$$

where L_P is a kinetic coefficient related to FE domain wall mobility.[20] F is the total free energy of the BTO crystal,

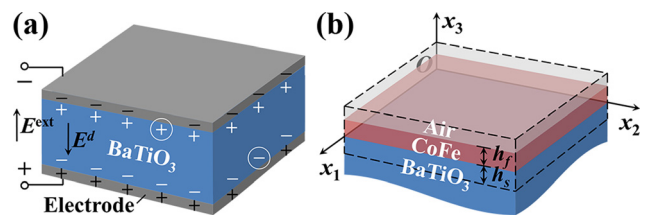

FIG. 1. (a) Schematics of the simulation system in Step 1 of the phase-field model: determining FE domain structures in a fully electroded BTO crystal substrate with uncompensated bound charges (see the circle) (b) Step 2: determining magnetic domain structures in the CoFe film in a film-substrate system. The simulation zone is marked by dashed lines, where a unique displacement boundary condition relating to polarization distribution [Eq. (10)] is applied at the bottom of the substrate at $x_3 = -h_s$.

a)E-mail: tuy123@psu.edu

$F = F_{\text{Landau}} + F_{\text{gradient}} + F_{\text{elec}} + F_{\text{elastic}}$. Here, F_{Landau} and F_{gradient} are the FE bulk free energy and FE gradient energy, respectively, with mathematic expressions given in Refs. 21 and 22. F_{elec} is the electrostatic energy

$$F_{\text{elec}} = \int \left(-\frac{1}{2} E_i^d P_i - E_i^{\text{ext}} P_i \right) dV, \tag{2}$$

where $\mathbf{E}^d$ and $\mathbf{E}^{\text{ext}}$ denote the depolarization field and the external electric field, respectively; summation conventions over repeat indices ($i = 1,2,3$) are employed. A mixed electrostatic boundary is considered in solving $\mathbf{E}^d$, in which the bound charges at the top and bottom electrodes are partly compensated [Fig. 1(a)], through treating the depolarization field as the sum of a heterogeneous field $\mathbf{E}^{d,A}$ and a homogeneous field $\mathbf{E}^{d,B}$, i.e., $\mathbf{E}^d = \mathbf{E}^{d,A} + \mathbf{E}^{d,B}$. $\mathbf{E}^{d,A}$ is calculated by numerically solving the electrostatic equation

$$\kappa_0 \kappa^b \frac{\partial E_i^d}{\partial x_i} + \frac{\partial P_i}{\partial x_i} = 0, \tag{3}$$

using a short-circuit condition[22] on top and bottom boundaries, where κ_0 and κ^b are the vacuum and background[23] dielectric permittivity, respectively. $\mathbf{E}^{d,B}$ is given by $\mathbf{E}^{d,B} = -k\bar{\mathbf{P}}/(\kappa_0 \kappa_b)$, in which $\bar{\mathbf{P}}$ is the average polarization in the system, and k is a factor determined by both the shape of the BTO substrate and the fraction of uncompensated bound charges, which would affect the volume fraction of in-plane and out-of-plane FE domains at the remnant state. Here, k is taken as 1% to describe the presence of a small fraction of uncompensated bound charges at the electrode/BTO interface. The elastic energy F_{elastic} is expressed as

$$F_{\text{elastic}} = \frac{1}{2} \int c_{ijkl} \left(\varepsilon_{ij} - \varepsilon_{ij}^0 \right) \left(\varepsilon_{kl} - \varepsilon_{kl}^0 \right) dV, \tag{4}$$

where $\mathbf{c}$ is the elastic stiffness tensor and $\boldsymbol{\varepsilon}$ the total strain. ε_{ij}^0 ($=Q_{ijkl}P_kP_l$, $\mathbf{Q}$ denoting the electrostrictive coefficient tensor) is the stress-free (or ferroelastic herein) strain during FE phase transitions (e.g., appearance of spontaneous polarization and polarization switching). The total strain $\boldsymbol{\varepsilon}(\mathbf{x})$ is numerically solved based on Khachaturyan's mesoscopic elasticity theory[24] under a 3D periodic stress-free boundary condition. The evolution of FE domains [Eq. (1)] is solved numerically using the semi-implicit Fourier spectral method.[25] Material parameters for the BTO bulk crystal are listed in Refs. 26–29.

The ferroelastic strains in the BTO substrate include (1) the structural strain from the cubic to tetragonal phase transition that can be partly transferred to CoFe film during its growth;[4] and (2) the electric-field-induced strain during 90° FE domain switching,[30] which normally can be fully transferred to the CoFe film.[31,32] As mentioned above, spatial distribution of such ferroelastic strains will be used as the elastic boundary condition of the substrate (see discussion later) in Step 2 for simulating magnetic domain evolution in the CoFe film. The simulation zone of the film-substrate system [Fig. 1(b)] is discretized into a 3D array of $160 \times 160 \times 32$ cells, wherein 12 layers of CoFe are placed over 15 layers of BTO substrate and the uppermost 5 layers are air. The size of each cell is taken as $5 \times 5 \times 1\,\text{nm}^3$, and hence the thicknesses of the CoFe film (i.e., h_f) and the top layers of BTO substrate (i.e., h_s) are 12 nm and 15 nm, respectively. Three sets of order parameters are used to describe such CoFe-BTO system, including a local polarization field $\mathbf{P}(\mathbf{x})$, a local magnetization field $\mathbf{M}(\mathbf{x}) = M_s\mathbf{m}(\mathbf{x})$, where M_s is the saturation magnetization and $\mathbf{m}$ the normalized magnetization, and a phase field variable $\eta(\mathbf{x})$ describing the spatial distribution of the two phases, with $\eta(\mathbf{x}) = 1$ in the CoFe film and $\eta(\mathbf{x}) = 0$ in the BTO substrate.

The temporal evolution of the magnetization field is described by the Landau-Lifshitz-Gilbert equation, i.e.,

$$(1+\alpha^2)\frac{\partial \mathbf{M}}{\partial t} = -\gamma_0 \mathbf{M} \times \mathbf{H}_{\text{eff}} - \frac{\gamma_0 \alpha}{M_s} \mathbf{M} \times (\mathbf{M} \times \mathbf{H}_{\text{eff}}), \tag{5}$$

where α is the damping constant, γ_0 is the gyromagnetic ratio, and $\mathbf{H}_{\text{eff}}$ is the effective magnetic field, given by $\mathbf{H}_{\text{eff}} = -(1/\mu_0)(\delta F/\delta \mathbf{M})$. The free energy F for CoFe is calculated as $F = F_{\text{exch}} + F_{\text{ms}} + F_{\text{external}} + F_{\text{elastic}}$, where F_{exch}, F_{ms}, and F_{external} are the magnetic exchange energy, magnetostatic energy, and external magnetic field energy, respectively, with the same formulations as in Ref. 33. The expression of elastic energy F_{elastic} is the same as Eq. (4), but here the stress-free strain ε_{ij}^0 is written as

$$\varepsilon_{ij}^0 = \begin{cases} \eta \left[\frac{3}{2} \lambda_s \left(m_i m_j - \frac{1}{3} \right) \right] + (1-\eta) Q_{ijkl} P_k P_l, & i = j \\ \eta \left(\frac{3}{2} \lambda_s m_i m_j \right) + (1-\eta) Q_{ijkl} P_k P_l, & i \neq j \end{cases} \tag{6}$$

where λ_s is the saturation magnetostriction, and the polarization field distribution $\mathbf{P}$ relating to the ferroelastic strain $Q_{ijkl}P_kP_l$ is taken from that in the top layers of the BTO substrate from Step 1. The total strain is calculated as the sum of a homogeneous strain $\bar{\boldsymbol{\varepsilon}}$ and a heterogeneous strain $\boldsymbol{\varepsilon}^{\text{het}}(\mathbf{x})$, i.e., $\boldsymbol{\varepsilon}(\mathbf{x}) = \bar{\boldsymbol{\varepsilon}} + \boldsymbol{\varepsilon}^{\text{het}}(\mathbf{x})$. Here, $\bar{\boldsymbol{\varepsilon}}$ (including $\overline{\varepsilon_{11}}$, $\overline{\varepsilon_{22}}$, and $\overline{\varepsilon_{12}}$) are calculated as $\overline{\varepsilon_{ij}} = \overline{\varepsilon_{ij}^{\text{BTO}}} - r\overline{\varepsilon_{ij}^{\text{BTO,growth}}}$ $(i,j=1,2)$, where $\overline{\boldsymbol{\varepsilon}^{\text{BTO,growth}}}$ and $\overline{\boldsymbol{\varepsilon}^{\text{BTO}}}$ are the volume averages of the spatially varying strain $\boldsymbol{\varepsilon}(\mathbf{x})$ within the top 15 layers of the BTO substrate during film growth and under the applied electric field, respectively, taken from Step 1, and r is the fraction of the relaxed strain taken as 0.9 according to experimental measurements.[4] In doing so, both the partial relaxation of the initial structural strain during the magnetic thin film growth and the full transfer of electric-field-induced strain are incorporated. The heterogeneous strain $\boldsymbol{\varepsilon}^{\text{het}}$, the volume average of which is zero,[33] is computed as

$$\varepsilon_{ij}^{\text{het}} = \frac{1}{2} \left(\frac{\partial u_i}{\partial x_j} + \frac{\partial u_j}{\partial x_i} \right). \tag{7}$$

Here, $\mathbf{u}(\mathbf{x})$ is the spatial distribution of local displacements, which can be obtained by solving the elastic equilibrium equation $\partial \sigma_{ij}/\partial x_j = 0$, expanded as

$$c_{ijkl} \frac{\partial^2 u_k}{\partial x_l \partial x_j} = c_{ijkl} \frac{\partial \varepsilon_{kl}^0}{\partial x_j}. \tag{8}$$

Note that a stress-free boundary condition is applied at the top surface of the film [$x_3 = h_f$, see Fig. 1(b)], i.e.,

$$c_{i3kl}\frac{\partial u_k}{\partial x_l}\bigg|_{x_3=h_f} = c_{i3kl}\varepsilon^0_{kl}\bigg|_{x_3=h_f}, \quad (9)$$

while a displacement boundary condition is imposed at the bottom of the substrate ($x_3 = -h_s$, see Fig. 1), expressed as[34]

$$u_i|_{x_3=-h_s} = u_i^{\mathrm{BTO}} - ru_i^{\mathrm{BTO,growth}} \quad (i=1,2,3), \quad (10)$$

where $\mathbf{u}^{\mathrm{BTO,growth}}$ and $\mathbf{u}^{\mathrm{BTO}}$ are the displacement distributions in the top layers of the BTO substrate during film growth and under the applied electric field, respectively. Eq. (8) is solved by utilizing a superposition methodology.[34] The evolution of magnetic domains [Eq. (5)] is solved numerically using semi-implicit Fourier spectral method[25] and Gauss-Seidel projection method.[35] Material parameters of CoFe are listed in Refs. 36–39.

Utilizing the above-described phase-field model, we can easily reproduce the experimentally observed[3,4] pattern copy between the elastically coupled magnetic and FE domains in the CoFe-BTO heterostructure. As illustrated in the first column in Fig. 2(a), alternating a_1 and a_2 in-plane FE domains with orthogonal polarizations are stabilized in the BTO substrate before electric field poling, similar as those in experiments.[3–5] This pattern is precisely imprinted to the overlaying CoFe film during its growth through local elastic coupling. Such elastic modulation of the magnetic domains can be interpreted based on the difference between the two in-plane normal strain components, i.e., ε_{11}-ε_{22}, which determines the orientations of magnetic easy axes in the CoFe film. Specifically, an alternating distribution of positive and negative ε_{11}-ε_{22} ($\sim$1% and -1%) are generated corresponding to the alternating FE a_1 and a_2 domains in the BTO substrate [see the first column in Fig. 2(b)], respectively, which are partly (10%[4] for $r = 0.9$) transferred to the top CoFe film [see the first column in Fig. 2(c)]. Such striped strain field induces the observed one-to-one match between the FE and magnetic domains,[3–5] e.g., a_1(FE) to a_1(magnetic), and a_2(FE) to a_2(magnetic), due to the positive λ_s of $Co_{0.6}Fe_{0.4}$.[37]

We next show the electric-field manipulation of magnetic domain pattern in such elastically coupled CoFe-BTO heterostructure. An electric field along the out-of-plane x_3 direction, E_3, is applied to the system, which cycles linearly between 0 and 600 kV/m at a rate of 7 kV m^{-1} ns^{-1}. Upon increasing electric field, the initial in-plane a_1/a_2 stripe domains in the BTO substrate gradually rotate off the plane and eventually become an out-of-plane c single-domain at $E_3 = 600$ kV/m [see the second column in Fig. 2(a)]. During this process, the strain field at the surface of BTO changes from a striped pattern [see the first column in Fig. 2(b)] to an isotropic ($\varepsilon_{11} - \varepsilon_{22} \approx 0$) uniform distribution [see the second column in Fig. 2(b)], thereby the initial FE a_1 and a_2 domain regions undergoing the strain changes [i.e., $\Delta(\varepsilon_{11}$-$\varepsilon_{22})$] of about -1% and 1%, respectively. These electric-field-induced strain changes at the BTO top surface are fully transferred to the overlaying CoFe film with an initial strain distribution shown in the first column in Fig. 2(c), resulting in a new striped strain field with ε_{11}-$\varepsilon_{22} \approx \mp 0.9$% as shown by the second column in Fig. 2(c). Accordingly, magnetic a_2 and a_1 domains are induced on top of the initial FE a_1 and a_2

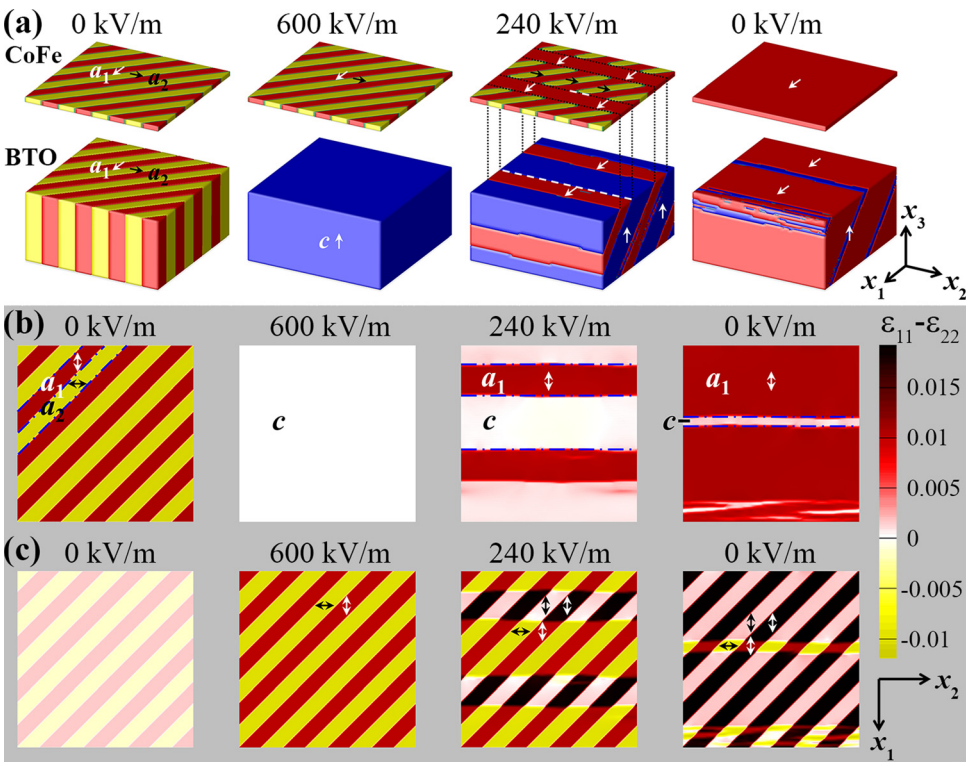

FIG. 2. (a) FE domain configuration of the BTO substrate and magnetic domain configuration of the CoFe film upon increasing E_3 from 0 (first column) to 600 kV/m (second column), followed by reducing E_3 to 240 kV/m (third column) and then to 0 (fourth column). The arrows indicate the directions of local polarization/magnetization vectors. Domain definitions and the corresponding polarizations/magnetizations: a_1: (P_1, 0, 0) or (m_1, 0, 0); a_2: (0, P_2, 0) or (0, m_2, 0); c: (0, 0, P_3) or (0, 0, m_3). Corresponding distributions of the in-plane strain difference ε_{11}-ε_{22} at (b) the top surfaces of the original BTO substrate and (c) the CoFe film. The dashed lines indicate boundaries of the FE domains. The double-headed arrows indicate the elongated in-plane axes.

domain regions, respectively, leading to a pattern interchange of the original magnetic a_1 and a_2 domain regions [see the second column in Fig. 2(a)].

Subsequent decrease of E_3 induces the formation and growth of in-plane FE a_1 domains in the BTO substrate, presenting a multi-domain a_1/c structure [see the third column in Fig. 2(a)]. The development of FE a_1 domains is associated with an in-plane strain change, $\Delta(\varepsilon_{11}\text{-}\varepsilon_{22})$, of 1.0%, leading to the striped strain field of $\varepsilon_{11}\text{-}\varepsilon_{22} \approx 0.1\%$ and 1.9% within the regions of initial FE a_1 and a_2 domains at the BTO surface, respectively [see the third column in Fig. 2(b)]. The corresponding strain distribution in CoFe film is illustrated by the third column in Fig. 2(c), where variations take place on top of the newly developed FE a_1 domain and would favor an alignment of a magnetic a_1 domain as $\lambda_s > 0$. By contrast, the magnetic stripe domain on top of FE c domains is preserved, leading to a mixed a_1 and striped a_1/a_2 domain pattern in the CoFe film [see the third column in Fig. 2(a)]. As E_3 further decreases, the induced magnetic a_1 domain keeps growing with the expansion of its elastically coupled FE a_1 domain underneath, eventually exhibiting a magnetic a_1 single domain at $E_3 = 0$ [see the fourth column in Fig. 2(a)]. An increase of E_3 back to 600 kV/m brings back the magnetic a_1/a_2 stripe domain in CoFe film and the FE c single domain in BTO substrate exactly as shown by the second column in Fig. 2(a). Such repeatable electric-field writing and erasure of magnetic striped a_1/a_2 domains have been demonstrated by experimental observations.[4]

A close examination on the dynamics of the magnetic domain evolution reveals an alternating occurrence of local magnetization rotation and domain wall motion associated with the FE domain evolution. In the downhill electric-field cycle, when the width of the newly formed FE a_1 domains is small, the magnetic stripe pattern remains unchanged, i.e., new magnetic a_1 domain does not form on top of the FE a_1 domain. When the underlying FE a_1 domain reaches a critical width of around 70 nm at $E_3 = 280$ kV/m, the magnetic striped a_1/a_2 domain above FE a_1 domain starts transforming into a magnetic a_1 domain through a coherent magnetization rotation of 90° [see Fig. 3(c)] as the ferroelastic strain-induced magnetic anisotropy is sufficiently large to overcome the exchange and magnetostatic energy penalty. Detailed magnetic free energy analysis for such finite-size scaling of domain pattern transfer has been reported in a recent study.[10]

Such transformation from local magnetic a_1/a_2 to a_1 domain is complete as the E_3 decreases to 260 kV/m, at which the newly developed magnetic a_1 domain are wider and gets coupled to the underlying FE a_1 domain. From the moment on, the evolution of the mixed a_1 and a_1/a_2 magnetic domains closely tracks the FE domain evolution through the motion of the elastically coupled magnetic and FE domain walls. For illustration, we select a certain magnetic a_1/a_2 domain wall and the associated FE a_1/c domain wall [as indicated by the white dashed lines in the third column of Fig. 2(a)] and track their velocities along the x_1 direction, as demonstrated in Fig. 3(a). The domain wall positions are located where $P_1 = P_3$ for a FE a_1/c domain wall and $m_1 = m_2$ for a magnetic a_1/a_2 domain wall [as an example, see Fig. 3(b) for the domain wall configurations at

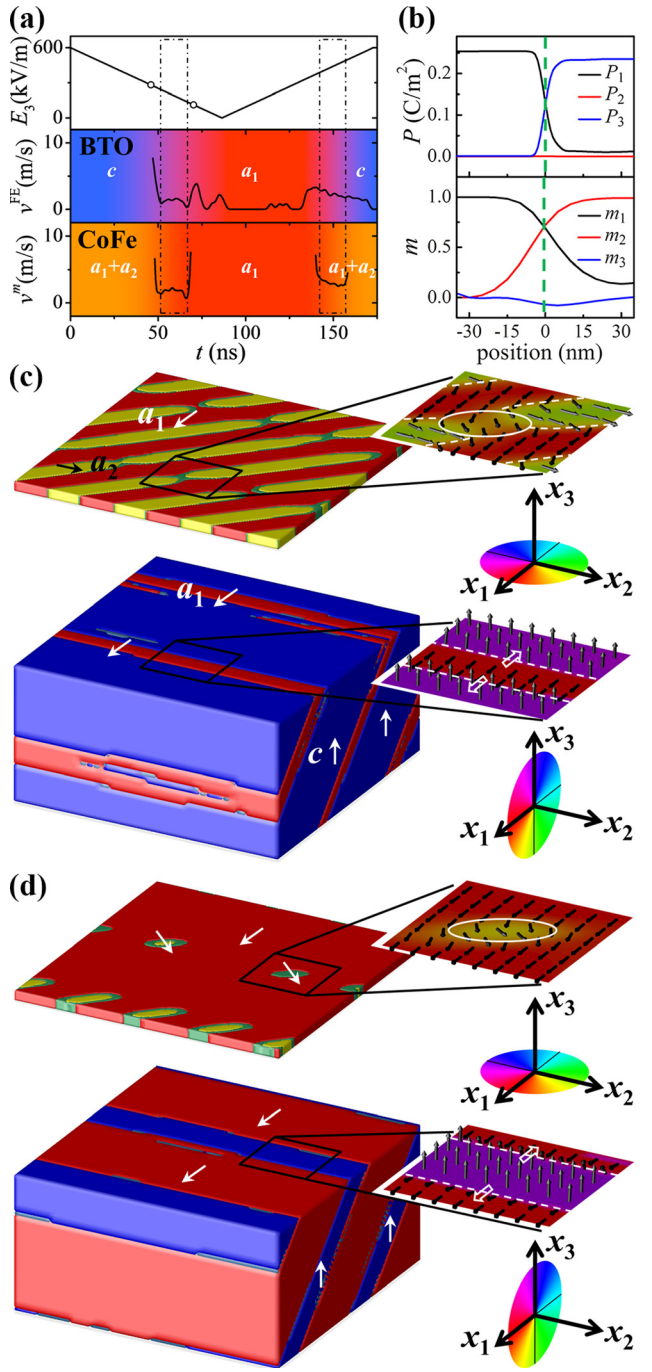

FIG. 3. (a) (Top) time sequence of the applied out-of-plane electric field E_3, and the velocities of (middle) FE and (bottom) magnetic domain wall motion, in FE a_1/c domain and mixed a_1 and a_1/a_2 magnetic domain configurations, respectively. The regions encircled by dashed-dotted lines indicate the coupled domain wall motion, and the background colors indicate the dominant FE or magnetic domains at different stages. (b) (Top) polarization and (bottom) magnetization configurations across the selected FE and magnetic domain walls, respectively, at $E_3 = 240$ kV/m in the downhill cycle. The dashed lines indicate the domain wall positions. Magnetic and FE domain structures at (c) $E_3 = 280$ kV/m and (d) $E_3 = 110$ kV/m in a downhill electric-field cycle. (Right columns) close-up vector plots of the polarization and magnetization configuration within the selected areas; the white dashed lines and the hollow arrows indicate the domain wall and the direction of the domain wall motion, respectively; the white solid circles indicate the regions undergoing magnetization rotation.

$E_3 = 240$ kV/m]. As seen, the velocity of the magnetic a_1/a_2 domain wall is almost identical to the FE domain wall from $E_3 = 250$ kV/m to $E_3 = 130$ kV/m [see the region encircled

by dashed-dotted lines in Fig. 3(a)]. Upon further reducing E_3 from 130 kV/m when the width of FE c domains reduces to about 110 nm, the a_2 domain rapidly shrinks, becoming decoupled from the underlying FE c domains due to the reduction of the ferroelastic strain-induced magnetic anisotropy. Such decoupling of magnetic a_2 and FE c domain is another manifestation of the finite-size scaling of the domain pattern transfer besides the onset of magnetic a_1-to-FE a_1 domain coupling at $E_3 = 260$ kV/m. Indeed, the local a_2 domain starts transforming into a magnetic a_1 domain through a coherent magnetization rotation [e.g., see Fig. 3(d) at which $E_3 = 110$ kV/m] and eventually vanishes, creating a uniform a_1 single domain in the whole CoFe film. Similar domain evolution behaviors are observed in the subsequent uphill electric-field cycle.

In conclusion, a phase-field model has been developed to study the local elastic coupling behaviors of the magnetic and FE domains in a multiferroic heterostructure of a magnetic film grown on a FE substrate. Taking a polycrystalline CoFe and a BTO crystal as an example, the one to one match of the initial magnetic and FE domain structures and the repeated electric-field writing and erasure of the magnetic striped domains have been simulated, providing modeling supplement and theoretical insights to experimental observations. Studies on the dynamics of the electric-field driven magnetic domain evolution reveal an alternating occurrence of local magnetization rotation and the coupled motion of magnetic and FE domain walls with almost identical velocities.

The authors are grateful for the financial support from the National Science Foundation (Grant Nos. DMR-1006541 and DMR-0820404), the NSF of China (Grant Nos. 51332001, 51221291, and 11234005). The computer simulations were performed on the LION and Cyberstar Computing Systems at the Pennsylvania State University supported in part by NSF Major Research Instrumentation Program through Grant OCI-0821527 and in part by the Materials Simulation Center and the Graduated Education and Research Services at the Pennsylvania State University.

[1]A. Schilling, T. B. Adams, R. M. Bowman, J. M. Gregg, G. Catalan, and J. F. Scott, Phys. Rev. B **74**, 024115 (2006).
[2]G. Catalan, J. F. Scott, A. Schilling, and J. M. Gregg, J. Phys.: Condens. Matter **19**, 022201 (2007).
[3]T. H. E. Lahtinen, J. O. Tuomi, and S. van Dijken, Adv. Mater. **23**, 3187–3191 (2011).
[4]T. H. E. Lahtinen, K. J. A. Franke, and S. van Dijken, Sci. Rep. **2**, 258 (2012).
[5]T. H. E. Lahtinen, Y. Shirahata, L. Yao, K. J. A. Franke, G. Venkataiah, T. Taniyama, and S. van Dijken, Appl. Phys. Lett. **101**, 262405 (2012).
[6]R. V. Chopdekar, V. K. Malik, A. F. Rodríguez, L. Le Guyader, Y. Takamura, A. Scholl, D. Stender, C. W. Schneider, C. Bernhard, F. Nolting, and L. J. Heyderman, Phys. Rev. B **86**, 014408 (2012).
[7]R. Streubel, D. Köhler, R. Schäfer, and L. M. Eng, Phys. Rev. B **87**, 054410 (2013).
[8]S. Geprägs, M. Opel, S. T. B. Goennenwein, and R. Gross, Phys. Rev. B **86**, 134432 (2012).
[9]S. Geprägs, D. Mannix, M. Opel, S. T. B. Goennenwein, and R. Gross, Phys. Rev. B **88**, 054412 (2013).
[10]K. J. A. Franke, D. L. González, S. J. Hämäläinen, and S. van Dijken, Phys. Rev. Lett. **112**, 017201 (2014).
[11]K. J. A. Franke, T. H. E. Lahtinen, and S. van Dijken, Phys. Rev. B **85**, 094423 (2012).
[12]H. T. Chen, Y. Ni, and A. K. Soh, J. Appl. Phys. **113**, 134102 (2013).
[13]V. V. Kruglyak, S. O. Demokritov, and D. Grundler, J. Phys. D: Appl. Phys. **43**, 264001 (2010).
[14]J.-M. Hu, Z. Li, L. Q. Chen, and C.-W. Nan, Nat. Commun. **2**, 553 (2011).
[15]J.-M. Hu, Z. Li, L. Q. Chen, and C.-W. Nan, Adv. Mater. **24**, 2869–2873 (2012).
[16]N. Lei, T. Devolder, G. Agnus, P. Aubert, L. Daniel, J.-V. Kim, W. Zhao, T. Trypiniotis, R. P. Cowburn, C. Chappert, D. Ravelosona, and P. Lecoeur, Nat. Commun. **4**, 1378 (2013).
[17]J. Dean, M. T. Bryan, T. Schrefl, and D. A. Allwood, J. Appl. Phys. **109**, 023915 (2011).
[18]L. Q. Chen, Annu. Rev. Mater. Res. **32**, 113 (2002).
[19]L. Q. Chen, J. Am. Ceram. Soc. **91**, 1835–1844 (2008).
[20]J. Hlinka, Ferroelectrics **349**, 49–54 (2007).
[21]Y. L. Li, S. Y. Hu, Z. K. Liu, and L. Q. Chen, Appl. Phys. Lett. **78**, 3878 (2001).
[22]Y. L. Li, S. Y. Hu, Z. K. Liu, and L. Q. Chen, Appl. Phys. Lett. **81**, 427 (2002).
[23]A. K. Tagantsev, Ferroelectrics **375**, 19–27 (2008).
[24]A. G. Khachaturyan, *Theory of Structural Transformation in Solids* (Wiley, New York, 1983).
[25]L. Q. Chen and J. Shen, Comput. Phys. Commun. **108**, 147 (1998).
[26]$\alpha_1 = 8.0 \times 10^7 \times [1/\tanh(160/T) - 1/\tanh(160/390)]$, $\alpha_{11} = -1.154 \times 10^8$, $\alpha_{12} = 6.530 \times 10^8$, $\alpha_{111} = -2.106 \times 10^9$, $\alpha_{112} = 4.091 \times 10^9$, $\alpha_{123} = -6.688 \times 10^9$, $\alpha_{1111} = 7.59 \times 10^{10}$, $\alpha_{1112} = -2.193 \times 10^{10}$, $\alpha_{1122} = -2.221 \times 10^{10}$, $\alpha_{1123} = 2.416 \times 10^{10}$, $Q_1 = 0.11$, $Q_2 = -0.045$, $Q_4 = 0.029$ [Ref. 27], $\kappa^b = 10$ [Ref. 23], $s_{11} = 9.1 \times 10^{-12}$, $s_{12} = -3.2 \times 10^{-12}$, $s_{44} = 8.2 \times 10^{-12}$ [Refs. 28 and 29] (in SI units).
[27]J. J. Wang, P. P. Wu, X. Q. Ma, and L. Q. Chen, J. Appl. Phys. **108**, 114105 (2010).
[28]D. Berlincourt and H. Jaffe, Phys. Rev. **111**, 143 (1958).
[29]A. F. Devonshire, Philos. Mag. **42**, 1065 (1951).
[30]J.-M. Hu, T. N. Yang, L. Q. Chen, and C. W. Nan, J. Appl. Phys. **113**, 194301 (2013).
[31]T. H. E. Lahtinen and S. van Dijken, Appl. Phys. Lett. **102**, 112406 (2013).
[32]J.-Y. Kim, L. Yao, and S. van Dijken, J. Phys.: Condens. Matter **25**, 082205 (2013).
[33]J.-M. Hu, T. N. Yang, L. Q. Chen, and C. W. Nan, J. Appl. Phys. **114**, 164303 (2013).
[34]Y. L. Li, S. Y. Hu, Z. K. Liu, and L. Q. Chen, Acta Mater. **50**, 395–411 (2002).
[35]X.-P. Wang, C. J. García-Cervera, and W. E, J. Comput. Phys. **171**, 357 (2001).
[36]$M_s = 19.099 \times 10^5$, $\lambda_s = 1.39 \times 10^{-4}$ [Ref. 37], $\alpha = 0.025$ [Ref. 38], $c_{11} = 257 \times 10^9$, $c_{12} = 162 \times 10^9$, $c_{44} = 105 \times 10^9$ [Ref. 39] (in SI units).
[37]R. C. Hall, J. Appl. Phys. **31**, S157 (1960).
[38]T. Maruyama, Y. Shiota, T. Nozaki, K. Ohta, N. Toda, M. Mizuguchi, A. A. Tulapurkar, T. Shinjo, M. Shiraishi, S. Mizukami *et al.* Nat. Nanotechnol. **4**, 158 (2009).
[39]J.-M. Hu, Z. Li, J. Wang, and C. W. Nan, J. Appl. Phys. **107**, 093912 (2010).